GdVO$_4$:Eu^{3+},Bi^{3+} Nanoparticles as a Contrast Agent for MRI and Luminescence Bioimaging

Guannan Zhu,[†,¶] Liping Chen,[‡,¶] Fanxin Zeng,[§,∥,¶] Lei Gu,[†,⊥] Xuefeng Yu,[#] Xue Li,[⊥] Jing Jiang,[†] Gang Guo,[⊥] Jiayi Cao,[†] Ke Tang,[†] Hongyan Zhu,[⊥] Heike E. Daldrup-Link,[∥] and Min Wu*[,†,§,∥]

[†]Huaxi MR Research Center (HMRRC), Department of Radiology, West China Hospital, [‡]Department of Biliary Surgery, West China Hospital, and [⊥]Laboratory of Stem Cell Biology, State Key Laboratory of Biotherapy, West China Hospital, Sichuan University, Chengdu 610041, China

[§]Department of Clinic Medical Center, Dazhou Central Hospital, Dazhou 635000, China

[∥]Department of Radiology, Molecular Imaging Program at Stanford (MIPS), Stanford University, 725 Welch Road, Stanford, California 94305, United States

[#]Institute of Biomedicine and Biotechnology, Shenzhen Institutes of Advanced Technology, Chinese Academy of Sciences, Shenzhen 518055, China

ABSTRACT: With the development of multifunctional imaging, gadolinium (Gd)-bearing inorganic nanoparticles (NPs), which were doped with trivalent lanthanide (Ln^{3+}), have been applied in magnetic resonance imaging (MRI) and optical imaging owing to their high payload of Gd^{3+} ions and specific optical characteristics. In this study, we chose GdVO$_4$ codoped with Eu^{3+} and Bi^{3+} as the host material to generate a highly efficient contrast agent (CA) for MRI and long-term luminescence imaging. The new CA emits strong and stable luminescence because of its strong characteristic emissions, resulting from the energy-transfer process from the vanadate groups (VO$_4^{3-}$) to the Eu^{3+} and Bi^{3+} dopants. Additionally, these NPs provided conspicuous T_1 and T_2 relaxation time-shortening characteristics, which result in MRI enhancement. GdVO$_4$:Eu^{3+},Bi^{3+} NPs were tested on liver tumor-bearing nude mice, and showed improved liver tumor contrast in T_2-weighted MR images (T_2WI). The dual-modal imaging probe exhibited no cytotoxicity or organ toxicity, reflecting its excellent biocompatibility. Thus, GdVO$_4$:Eu^{3+},Bi^{3+} has the potential to be used for bioassays *in vitro* and liver tumor targeting *in vivo*. The results reveal the great promise of using the designed GdVO$_4$:Eu^{3+},Bi^{3+} NPs as luminescent and MRI dual-mode bioprobes for clinical bioimaging applications.

1. INTRODUCTION

Molecular imaging has been applied in the development of precision medicine, where it has improved the accuracy of clinical diagnoses and treatments.[1−4] Contrast agents (CAs) composed of nanomaterials and organic materials are extensively applied to molecular imaging.[5−8] Using magnetic resonance imaging (MRI) to diagnose liver tumors is a good clinical choice.[9,10] Compared to routine MRI, current clinical MRI techniques for detecting hepatocellular carcinoma (HCC) achieve higher mean sensitivity and specificity (89.7% and 92%, respectively, compared with 84.9% and 89.7% for routine MRI) with standard small-molecule Gd chelates.[11] The optical imaging technique has significant advantages, such as excellent sensitivity, high resolution, contrast, instrument portability, and low cytotoxicity.[5] Moreover, multimodal imaging probes can provide more precise information for disease diagnosis and can be used to shuttle drugs into tumor tissue.[12]

Most of the available reports on different rare earth (RE) orthovanadate nanomaterials have focused on the YVO$_4$ and LaVO$_4$ platforms.[13−16] Because of the lackness of significant magnetic characteristics, the nanophosphors have been used only for biomedical applications, but they have not been used as MRI CAs.[16] Actually, gadolinium vanadate (GdVO$_4$) is an essential host matrix, which is widely used in near-infrared (NIR) light and activated RE oxide phosphors.[17,18] However, concerns have recently been raised about brain deposition of the small-molecule Gd chelates currently used in clinical practice.[19,20] Compared with commercial small-molecule Gd chelate complexes, Gd-based inorganic nanoparticles (NPs) incorporate Gd^{3+} ions into a solid structure rather than into organic molecules, effectively avoiding the possibility of dissociation and the consequent leakage of Gd^{3+} while minimizing related toxicity and increasing the proton relaxivity.[21] A series of inorganic Gd-based compounds have been used for MRI contrast enhancement, including
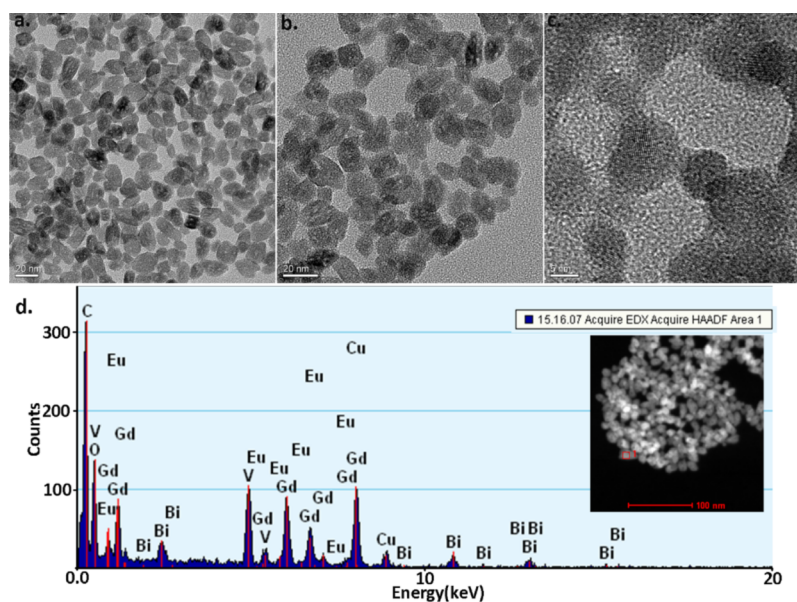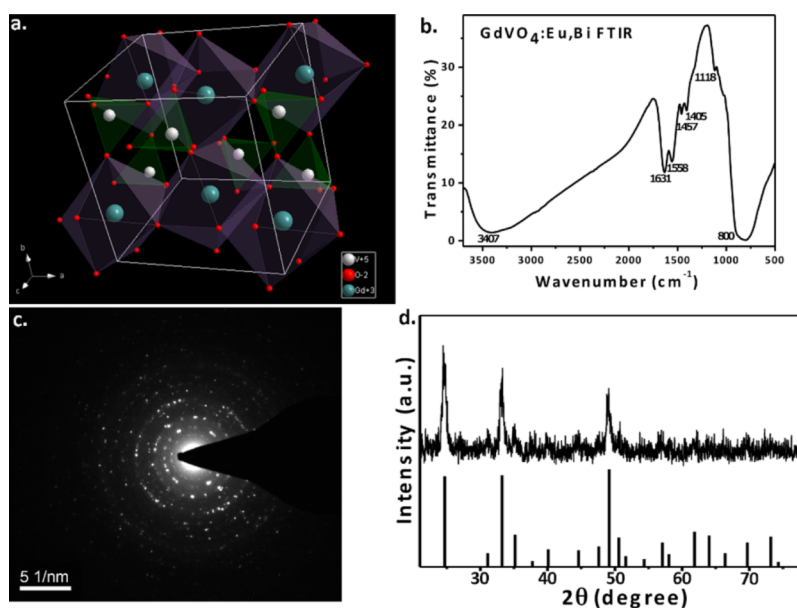
Figure 1. (a,b) TEM micrographs of GdVO$_4$:Eu^{3+},Bi^{3+} NP samples, scale bar = 20 nm. (c) High-magnification TEM micrograph of the NPs, scale bar = 5 nm. (d) EDS exhibiting the NPs elementary composition of the NPs.


Figure 2. (a) Schematic of the tetragonal-phase GdVO$_4$ structure (coordination mode). (b) FTIR spectrum of GdVO$_4$:Eu^{3+},Bi^{3+} NPs. (c) SAED pattern of GdVO$_4$:Eu^{3+},Bi^{3+} NPs. (d) XRD pattern of the GdVO$_4$:Eu^{3+},Bi^{3+} sample.

gadolinium oxides (Gd$_2$O$_3$),[22,23] gadolinium fluorides (GdF$_3$, NaGdF$_4$),[24−26] gadolinium hydroxides (Gd(OH)$_3$),[27] and gadolinium oxysalts (GdVO$_4$, GdPO$_4$).[28−30] Furthermore, in multifunctional imaging fields, these NPs are promising vehicles for carrying luminescence-imaging cations, especially trivalent lanthanide ions (Ln^{3+}). Notably, some of these new MRI CAs demonstrate both T_1 and T_2 relaxation time-shortening effects, and Gd-based NPs have a high r_2/r_1 ratio, with dominant T_2 signal enhancement.[31] GdVO$_4$ NPs have strong potential for multimodal MRI and luminescence imaging.

RE-based luminescent NPs, consisting of a host material which is doped with Ln ions, lack fluorescence scintillation, have excellent photostability, long lives, low cytotoxicity, and extraordinary narrow emission lines.[32] Gadolinium orthovana-date (GdVO$_4$)-based NPs can be doped with RE ions for luminescent displays because of their equal valences and similar ionic radii. When GdVO$_4$ is used as a host material, the [VO$_4$]$^{3−}$ groups strongly absorb UV light. In addition, trivalent europium (Eu^{3+}) ion-doped materials, with excellent red luminescence resulting from the $^5D_0$ to $^7F_2$ (620 nm) electric dipole emission transition in the visible light range, are highly suitable photoluminescent probes because of the long photoluminescence (PL) lifetime of Eu^{3+}.[33] However, the red emission of Eu^{3+} is primarily produced via downshifting luminescence (DSL) processes, which depend on excitation by UV radiation with short wavelengths (normally <300 nm), which limits the applications of such materials for bioimaging.[34,35] Bi^{3+} (bismuth) sensitizers improve the luminescence properties by shifting the excitation peak toward longer
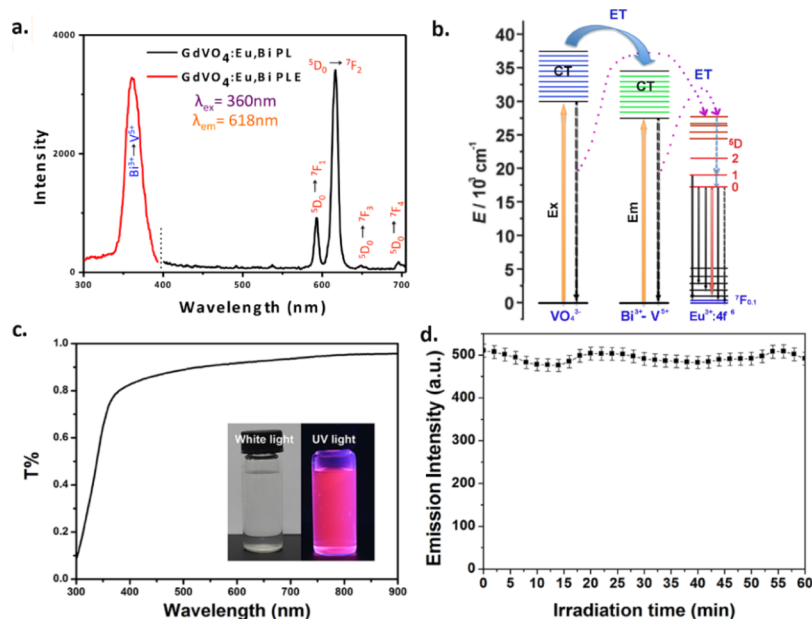
Figure 3. (a) PL excitation and emission spectrum (Ex = 360 nm, Em = 618 nm) of GdVO$_4$:Eu^{3+},Bi^{3+} NPs. (b) Schematic diagram of the proposed energetic processes occurring in the GdVO$_4$:Eu^{3+},Bi^{3+} samples. (c) Transmissivity spectrum of the samples; the inset shows the sample under near-UV-light and white-light excitation. (d) Luminescence time traces of the GdVO$_4$:Eu^{3+},Bi^{3+} NPs under UV-light irradiation for 1 h.

wavelengths.[36] In addition, Bi^{3+} functions as an activator when incorporated into the [VO$_4$]$^{3-}$ host material. With the 6s^2 electronic configuration, Bi^{3+} ions doped into REVO$_4$ materials doped with Bi^{3+} ions host active electrons that are first transferred from Bi^{3+} to the V^{5+} 3d^0 configuration and then to Eu^{3+}.[37,38]

Here, we present GdVO$_4$:Eu^{3+},Bi^{3+} NPs in which europium (Eu^{3+}) and bismuth (Bi^{3+}) are codoped into GdVO$_4$ NPs for detection with MRI and DSL bioimaging. The purpose of this study was to determine both the *in vitro* and *in vivo* bimodal imaging characteristics of this new CA.

2. RESULTS AND DISCUSSION

2.1. Synthesis and Structural Data. Figure 1a−c represents transmission electron microscopy (TEM) micrographs of the GdVO$_4$:Eu^{3+},Bi^{3+} NPs. The low-magnification TEM images (Figure 1a,b) displayed that the NPs exhibit an oval shape with a uniform size and are uniformly dispersed. The length of each particle is approximately 20−30 nm, and the width is approximately 10 nm. The structure of an individual NP that exhibits well-defined lattice fringes was depicted via high-magnification TEM micrograph (Figure 1c).

The purity of the NPs was investigated using energy-dispersive spectroscopy (EDS). Figure 1d presents an EDS spectrum of the sample. This result shows that the sample contains the elements of Gd, Bi, Eu, vanadium (V), and oxygen (O) (in Figure 1d, the elemental mapping image is shown in the small red box on the bottom-left of the inset), while the carbon (C) and copper (Cu) peaks emanate from the TEM carbon-coated copper grid. These EDS measurements demonstrate the successful incorporation of a high content of Eu^{3+} and Bi^{3+} ions into the nanocrystals.

Figure 2a is a graphic of the GdVO$_4$ crystal structure and the coordination mode for the tetragonal structure in which the Gd^{3+} and O^{2-} ions tetrahedrally coordinate with the V^{5+} cations in the spaces among the isolated VO$_4$ tetrahedral units. Therefore, Gd^{3+} ions and the surrounding eight O^{2-} ions

create a distorted GdO$_8$ dodecahedron. VO$_4$ tetrahedra and GdO$_8$ dodecahedra alternate and share edges, with Gd^{3+} and V^{5+} ions in a direct line that is parallel to the *c*-axis.[39,40]

In Figure 2c, the selected area electron diffraction (SAED) pattern displays a bright diffraction rosette are due to the (200), (220), and (400) crystal phases. Therefore, the NPs showed high crystallinity, forming a typical and pure tetragonal phase. In addition, in Figure 2d, the X-ray diffraction (XRD) patterns of the GdVO$_4$:Eu^{3+},Bi^{3+} consisting of peaks that follow the normal pattern of GdVO$_4$ (JCPDS, card no. 72-0277), including the presence of peaks corresponding to the GdVO$_4$, which has a cubic zircon crystal structure ($I4_1/amd$ space group).[37] The NPs are pure-phase GdVO$_4$ because no other peaks are observed.

A Fourier transform infrared (FTIR) spectroscopy absorption spectrum is shown in Figure 2b. The characteristic peak arising from the vanadium-oxygen stretching of tetrahedra appears at 800 nm; and this peak is known to appear in the region from 800 to 1050 cm^{-1}.[41] Peaks of 3400 and 1600 cm^{-1} result from the widening absorptions of water.

2.2. Optical Properties and Spectroscopic Data. Unfortunately, using UV excitation for *in vivo* imaging is limited by its uncaging process, which is very harmful, and it is difficult to apply this method to deep tissues because of the poor tissue penetration depth.[4,42] Downshifting emission excited by UV radiation (360 nm) cannot be effectively used for *in vivo* bioimaging limited by the greatly absorption of biological tissue in the UV spectral region (the quite short penetration length for the excitation radiation). In contrast, because of the advantages of NIR light, such as its tissue penetrability and low damage to cells and tissues, NIR light bands are ideal for biomedical applications.[43] The upconversion luminescence of Nd^{3+} can be excited and emitted at 808 nm, which is in the NIR range. It can achieve a higher signal-to-noise ratio and deeper tissue penetration when applied to small animal imaging.[44] Fortunately, phosphors could be excited by near-UV radiation, as the excitation peak of
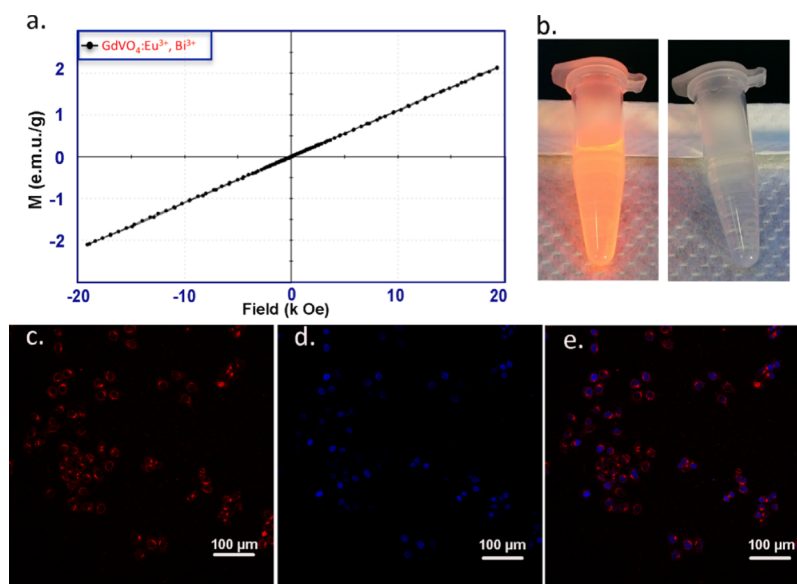
Figure 4. Magnetic properties of GdVO$_4$:Eu^{3+},Bi^{3+} NPs: (a) RT magnetization field ($M-H$) curve. (b) DLS fluorescence imaging under UV light (the right photo shows the control sample under visible light). Fluorescence images of HepG2 incubated with NPs: (c) TRITC channel, (d) DAPI channel, and (e) merged channels.
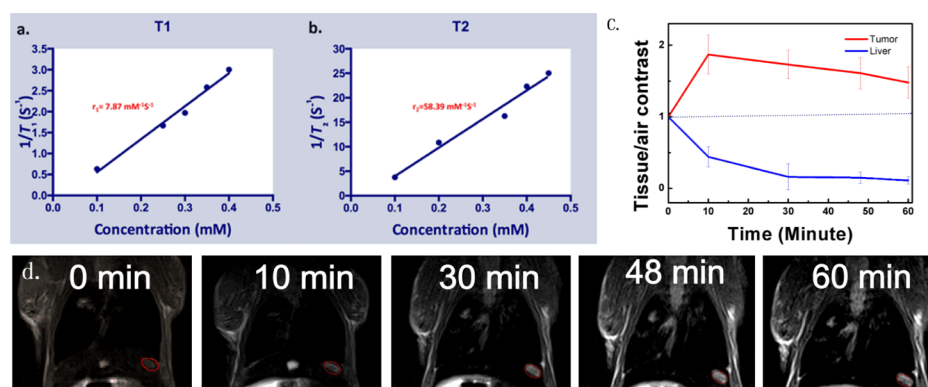
Figure 5. (a,b) Curves of longitudinal and transverse vs metal concentration of GdVO$_4$:Eu^{3+},Bi^{3+} NPs at 3.0 T. (c) Contrast intensities of the tumors, normal hepatic tissues compared with air. (d) T_2WI of tumor-bearing nude mice *in vivo* before (left: $t = 0$ min) and after (right) the injection of GdVO$_4$:Eu^{3+},Bi^{3+} NPs into the tail vein. The red circle shows the tumor site.

GdVO$_4$:Eu^{3+} can be shifted toward longer wavelengths if doped with Bi^{3+}.[34]

For luminescence imaging, the emission spectra and PL excitation of GdVO$_4$:Eu^{3+},Bi^{3+} were examined. GdVO$_4$ is a superb host material for downconversion because of its efficient energy transfer to the excited states of RE^{3+} dopants and strong absorption in the UV range.[40] The 280 nm excitation band is well known as the characteristic excitation spectral peak of GdVO$_4$:Eu^{3+}, on account of charge-transfer band from O^{2-} to V^{5+} within [VO$_4$]$^{3-}$ groups; subsequently energy is transferred to the Eu^{3+} cations.[34,43−46] The excitation spectra were because of the main emission line of Eu^{3+} ions in REVO$_4$ at 618 nm, and they were broadly examined in the near-UV range. In Figure 3a, the Bi^{3+} cations were introduced into the host lattice that leads to a new energy band, the maximum location of the wide absorption band, which is centered at approximately 360 nm. This shift can be explained by the appearance of the Bi^{3+} to V^{5+} CT process, following by energy transfer to Eu^{3+} cations.[47]

In Figure 3a, under UV excitation at 360 nm, emission spectra of the suspensions of the NPs displayed the characteristic transitions of Eu^{3+} cations from ^{5}D$_0$ to ^{7}F$_J$ (J = 1−4), and the ^{5}D$_0$ to ^{7}F$_2$ transition induces the highest intensity emission line at 618 nm.[33] The electric dipole transition ^{5}D$_0$ to ^{7}F$_2$ leads to the strong red light of GdVO$_4$:Eu^{3+},Bi^{3+} NPs. In addition, the schematic diagram of energy-transfer processes of different ions shown in the emission spectrum are displayed in Figure 3b.

The transmissivity (T) of the GdVO$_4$:Eu^{3+},Bi^{3+} NP solution is shown in Figure 3c, indicating that the light wavelength is broadened. Furthermore, under visible-light irradiation, the transmissivity of the material solution increased, and the T value approached 1. In accordance with the T value, the material solutions absorb near-UV light and emit red visible light (inset of Figure 3c).

To determine the photostability of the NPs, luminescence time traces of GdVO$_4$:Eu^{3+},Bi^{3+} NPs were obtained with 2 min bins under irradiation for 1 h. The result shows that no photobleaching was observed after constant irradiation, demonstrating the good photostability of the GdVO$_4$:Eu^{3+},Bi^{3+} NPs for long-term bioimaging (Figure 3d).
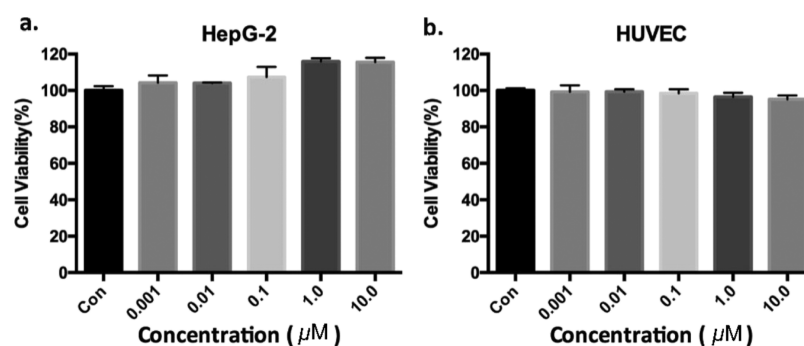
Figure 6. Viability of HepG2 cells (a) and HUVECs (b) after incubation with GdVO$_4$:Eu^{3+},Bi^{3+} NPs at increasing Gd concentrations. (a,b) Cell viability was measured by a CCK-8 array using the means and SD of the number of experiments per experimental group.
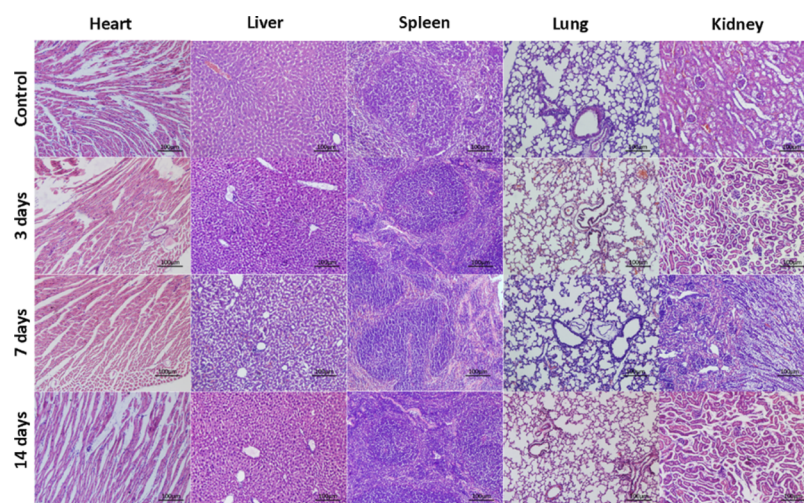
Figure 7. H&E-stained images of different organs after intravenous administration of GdVO$_4$:Eu^{3+},Bi^{3+} NPs into normal mice at 0, 3, 7, and 14 days (scale bar = 100 μm).

2.3. Cell Imaging. In Figure 4c−e, the uptake characteristics of the prepared NPs by HepG2 cells (human liver HCC cells) were tested by confocal laser-scanning microscopy, which was recorded by the tetramethylrhodamine (TRITC) channel. In the interior of the cells, a bright red emission was observed. This suggests that the HepG2 cells can be effectively taken up by the NPs. The results indicate that the NPs are suitable CAs for fluorescence imaging *in vitro*. However, the low emission wavelength of the NPs is not suitable for in-depth *in vivo* fluorescence imaging.[48]

2.4. Magnetic Properties and MRI Applications. To make the GdVO$_4$:Eu^{3+},Bi^{3+} NPs sufficiently compatible for further MRI applications, their magnetic properties were investigated with a vibrating sample magnetometer (VSM). As shown in Figure 6a, the room-temperature (RT) magnetization curve was linearly correlated with the magnetization intensity of 1.28 emu/g of NPs at 10 kOe, indicating that the NPs have potential applications in MRI.

Figure 5a,b shows *in vitro* T_1 and T_2 measurements for Gd^{3+}-doped RE NPs in aqueous suspensions with different Gd^{3+} concentrations. The literature contains many reports showing that Gd^{3+}-doped RE NPs have extremely low relaxivity, which limits their applications. In fact, most reports have focused on the T_1 contrast effect but not the T_2 contrast effect. Paramagnetic Gd-based MRI CAs exhibit increased signal intensity in the T_1-weighted images, so they are defined as "positive CAs".[50] Actually, Gd^{3+} ions have seven unpaired

electrons, which can generate large magnetic fluctuations, resulting in the shortening of the T_1 and T_2 values of the surrounding protons. In general, a low concentration of Gd^{3+} shortens the T_1 values, whereas extreme T_2 shortening occurs at high Gd^{3+} concentrations. The GdVO$_4$:Eu^{3+},Bi^{3+} NPs exhibit a high signal intensity, with an r_1 value of r_1 = 7.87 mM^{-1} s^{-1} and an r_2 value of 58.39 mM^{-1} s^{-1}. The r_2/r_1 ratio of the NPs was calculated as 7.42, indicating that the GdVO$_4$:Eu^{3+},Bi^{3+} NPs have potential applications as dual-weighted MRI CAs (both T_1 and T_2) for *in vivo* MRI,[49] although the high r_1 (r_1 = 7.87 mM^{-1} s^{-1}) of the GdVO$_4$:Eu^{3+},Bi^{3+} NPs was also observed. Obviously, the NPs' r_2/r_1 ratio is higher than the clinical value (r_2/r_1 ratio close to 1), primarily due to the T_2-shortening effect. Additionally, GdVO$_4$-related NPs have been mostly used as T_1-weighted CAs *in vitro* and *in vivo*,[28,51] and few studies on the applications of these NPs for T_2-weighted MRI have been conducted.

Therefore, for *in vivo* MRI studies, we concentrated on the function of the NPs as T_2 MRI CAs. As shown in Figure 5d, tumor-bearing BALB/c nude mice were intravenously injected at a dose of 10 mg of Gd per kg of mice body weight before recording by T_2WI. After injecting the CA, a significant decrease of approximately 44% at 10 min (instead of an increase) was observed in the signal strength of the hepatic parenchyma regions in T_2WI by measuring the signal intensities of the regions of tumor and liver regions, possibly

due to the effective uptake of NPs. Meanwhile, the tumor tissue showed an enhancement of 27% in the tumor at 10 min (Figure 5c), suggesting an obvious T_1 effect of the tumor tissue. This finding is consistent with previous reports of a lack of Kupffer cells in HCCs.[52,53]

2.5. Biocompatibility and Toxicity. Before GdVO$_4$:Eu^{3+},Bi^{3+} NPs can be used for *in vivo* multimodal imaging, toxicity testing is crucial. The NPs' cytotoxicity was evaluated by a Cell Counting Kit-8 (CCK-8) assay on HepG2 cells and human umbilical vein endothelial cells (HUVECs). HepG2 cells and HUVECs were incubated for 24 h in NP suspensions with NP concentrations ranging between 0 and 10 μM. In Figure 6, the change in proliferation was negligible for the treated cells.

To further evaluate the long-term safety of the GdVO$_4$:Eu^{3+},Bi^{3+} NPs, 20 healthy BALB/c mice were sacrificed and dissected at 0, 3, 7, and 14 days after intravenous administration with GdVO$_4$:Eu^{3+},Bi^{3+} NP suspension ($n = 5$, respectively). Histological analysis (in Figure 7) revealed that the organs (heart, spleen, liver, lung, and kidney) were normal. In addition, no deaths or behavioral changes were observed among the animals after NP administration, indicating that the GdVO$_4$:Eu^{3+},Bi^{3+} NPs are biocompatible.

3. EXPERIMENTAL SECTION

3.1. Materials. Fetal bovine serum (FBS) was purchased from Invitrogen (Carlsbad, CA). CCK-8 was acquired from Dojindo, Japan. Trypsin, phosphate-buffered saline (PBS) and RPMI 1640 medium were supplied by HyClone (Thermo, USA). Other reagents were obtained from Sinopharm Chemical Reagent Co. Ltd. (Shanghai, China). All chemicals were used as acquired without further purification. Ultrapure water was obtained from a Milli-Q water system.

3.2. NPs Synthesis. The GdVO$_4$:Eu^{3+},Bi^{3+} NPs were synthesized using our group's previously established method for preparing layered RE hydroxides.[53,54] During GdVO$_4$:Eu^{3+},Bi^{3+} NPs' synthesis, suitable amounts of the RE precursor LnCl$_3$ (Ln = Gd, Eu, Bi) were dissolved in ultrapure water to a concentration of 0.5 M. Under vigorous agitation, 1 mL of PEI solution (10% by weight) was added. The resulting solution was purged with nitrogen for 1 min to eliminate oxygen after stirring for another 5 min. The mixture was sealed into a 50 mL Teflon-lined autoclave, which was maintained at 200 °C for 2.5 h. The reaction mixture was stirred magnetically to remove the supernatant via centrifugation at 10 000 rpm for 5 min, after naturally cooling to RT. The precipitate was washed twice by ethanol and once with water and then redispersed with 5.0 mL Milli-Q water. Powder was obtained after the precipitate was dried for 12 h at 40 °C.

3.3. Characterization of the NPs. A transmission electron microscope (Tecnai G2 F20 S-TWIN, FEI, USA) was used to obtain the TEM micrographs of the GdVO$_4$:Eu^{3+},Bi^{3+} NPs. EDS coupled with TEM was used to analyze the element compositions of the NPs. An X'Pert Pro diffractometer (X'Pert Pro MPD DY129, PANalytical, Netherlands) was used to conduct XRD. The crystal structure was determined through SAED (XRD, AXIS Ultra DLD, UK). FTIR (Nicolet 6700, Thermo Fisher Scientific, USA) was used to characterize the samples. Fluorescence emission spectra of the NPs were observed on a Hitachi F-4500 fluorescence spectrophotometer equipped with a Xe lamp excitation source. The NPs' photostability was assessed by using a Cary 5000

UV−vis−NIR spectrometer to analyze the absorption spectra of immobilized NPs under continuous UV irradiation.

3.4. Cell Culture and Cytotoxicity Test. The HepG2 cell line and HUVEC line were supplied from the Cell Bank of the Chinese Academy of Sciences (Shanghai, China). The cells were incubated at 37 °C under 5% CO$_2$ atmosphere, with high-glucose Dulbecco's modified Eagle's medium (HyClone), within 1% streptomycin/penicillin (HyClone) and 10% FBS. A CCK-8 assay (Dojindo, Japan) was used to determine the *in vitro* cytotoxicity of the NPs. Briefly, 5 × 10^3 cells of the HepG2 cells or HUVECs were planted into 96-well plates. After seeding for 24 h, the cells were then exposed to NP solutions at different concentrations and cultured overnight. The gadolinium concentrations were 0, 0.001, 0.01, 0.1, 1.0, and 10.0 μM. The cells were then washed by PBS twice and tested by CCK-8 assay at 37 °C. The absorbance at 450 nm was measured using a Varioskan Flash microplate reader. Every result is reported as the average of six samples; the data are shown as the mean ± standard deviation (SD).

3.5. Cellular Uptake and Imaging. HepG2 cells were used to demonstrate the suitability of GdVO$_4$:Eu^{3+},Bi^{3+} NPs for bioimaging. Typically, the 2 × 10^5 HepG2 was incubated in each well of a 6-well plate with cover glasses for 24 h. Following, 1000 μg/mL NPs were added to each chamber after refreshing the growth medium. Then, cocultured for 2 h at 37 °C under a moist atmosphere of 5% CO$_2$. The cells were fixed in 4% paraformaldehyde solution for 15 min at RT after washing three times in PBS and then stained with a DAPI solution. The stained cells were washed and detected via confocal laser-scanning microscope (Ni-E, Nikon, Japan) with a 20× lens to obtain the luminescence images.

3.6. Establishment of a Liver Orthotopic Transplantation Tumor-Bearing Mouse Model. The animal experiment was conducted following the guidelines of the Animal Care and Use Committee of Sichuan University. Twenty male 7-week-old BALB/c nude mice, each weighed approximately 20 g, were acquired from the Institute of Experimental Animals, Sichuan Academy of Medical Sciences. HepG2 cells were harvested and resuspended in sterile PBS. For the orthotopic xenograft tumor model, mice were anesthetized via an intraperitoneal administration of chloral hydrate (10 wt %), and 1 × 10^6 HepG2 cells in 10 μL were injected slowly in the lower left lobe of the hepar (the largest one) after laparotomy directly.[55]

3.7. MR Relaxometry and *in Vivo* Imaging. The magnetization values of the NPs were measured by a VSM (Lake Shore 7410) at RT under an applied field ranging between 0 and 2.0 T. A 3.0 T clinical MRI instrument (Siemens Trio Tim) was performed to study *in vitro* MR relaxometry. To measure the MR relaxivity r_1 and r_2 values, the GdVO$_4$:Eu^{3+},Bi^{3+} NP solutions of different Gd^{3+} concentrations (0.1, 0.2, 0.3, 0.4, and 0.5 mM) in 4.0 mL test tubes in the PBS buffer containing 1% agarose were prepared.

Five mice with liver tumor xenografts underwent MRI with the rat coil on a 3.0 T MRI system (Siemens Trio Tim). The relevant MR parameters are as follows: T_2-weighted fast spin-echo, sequence: echo time (TE): 83 ms; repetition time (TR): 3000 ms; slice thickness: 1 mm; field of view: 60 × 60 cm^2; matrix: 320 × 320 pixels. After the tumor models were established, the mice were anesthetized with 10 wt % chloral hydrate, and 1 mmol Gd/mL of GdVO$_4$:Eu^{3+},Bi^{3+} NPs was injected intravenously via the tail at a concentration of 10 mg

Gd/kg mouse. Each mouse was scanned 0, 10, 30, 48, and 60 min after injection.

To quantify the contrast enhancement, ImageJ software was used to measure the signal intensity of interest in tumors and normal hepatic tissues. The signal intensities were compared after normalization.

3.8. *In Vivo* Toxicity Studies and Histological Analysis. Healthy male BALB/c mice were divided into four groups ($n = 5$ for each group) randomly, and 10 mg of Gd per kg mouse weight $GdVO_4:Eu^{3+},Bi^{3+}$ NP suspension was intravenously injected into the BALB/c mice through the tail vein for the three test groups ($n = 15$), and the control group ($n = 5$) was injected with 0.9 wt % NaCl.

To study the histologic changes, mice were sacrificed at 0, 3, 7, and 14 days after administration. The internal organs (liver, heart, spleen, lungs, and kidneys) were collected, fixed in 4% paraformaldehyde, and embedded in paraffin. The 5 μm-thick sections were evaluated with hematoxylin and eosin (H&E).

3.9. Statistical Analysis. All data are expressed as the mean ± SD. Every *in vitro* experiment was conducted in triplicate. *In vitro* data of different experimental groups were compared via a one-way analysis of variance and Student's *t*-test. *In vivo* data of different experimental groups were similarly compared. Statistical analysis was performed using Prism 6.0 software with $P < 0.05$, which indicates significant differences between experimental groups.

4. CONCLUSIONS

In conclusion, $GdVO_4$ NPs containing Eu^{3+} and Bi^{3+} ions are multimodal imaging agents that enable efficient MR T_2-weighted imaging and DSL luminescence imaging. The NPs can be excited in the near-UV and visible spectra ranges, and they have an excitation peak at 360 nm caused by the introduction of Bi^{3+} ions and an emission peak at 618 nm that is characteristic of the spectral profile of Eu^{3+}. Photostability experiments indicated that the NPs can provide luminescence images or enable cell monitoring *in vivo* in the long term. The relaxivity of these NPs demonstrated a 7.42 mM^{-1} s^{-1} high r_2/r_1 ratio for 3.0 T MRI, indicating that the NPs are suitable as a negative MRI CA. This observation conforms to the T_2WI. The negative contrast enhances the tumor-to-liver contrast in HCC-bearing mice. Furthermore, the good biocompatibility and low cytotoxicity of the NPs indicate their potential for biomedical applications.

AUTHOR INFORMATION

Corresponding Author
*E-mail: wuminscu@scu.edu.cn. Phone: +86-28-8542-2844. Fax: +86-28-8542-3503.

ORCID
Xuefeng Yu: 0000-0003-2566-6194
Gang Guo: 0000-0002-4440-6366
Min Wu: 0000-0002-7733-2498

Author Contributions
¶G.Z., L.C., F.Z. contributed equally.

Notes
The authors declare no competing financial interest.

ACKNOWLEDGMENTS

REFERENCES

(1) Yang, T.; Sun, Y.; Liu, Q.; Feng, W.; Yang, P.; Li, F. Cubic sub-20 nm $NaLuF_4$-based upconversion nanophosphors for high-contrast bioimaging in different animal species. *Biomaterials* **2012**, *33*, 3733−3742.

(2) Kwon, O. S.; Song, H. S.; Conde, J.; Kim, H.-i.; Artzi, N.; Kim, J.-H. Dual-color emissive upconversion nanocapsules for differential cancer bioimaging *in vivo*. *ACS Nano* **2016**, *10*, 1512−1521.

(3) Yang, Y.; Liu, F.; Liu, X.; Xing, B. NIR light controlled photorelease of siRNA and its targeted intracellular delivery based on upconversion nanoparticles. *Nanoscale* **2013**, *5*, 231−238.

(4) Jayakumar, M. K. G.; Idris, N. M.; Zhang, Y. Remote activation of biomolecules in deep tissues using near-infrared-to-UV upconversion nanotransducers. *Proc. Natl. Acad. Sci. U.S.A.* **2012**, *109*, 8483−8488.

(5) Chen, C.; Ou, H.; Liu, R.; Ding, D. Regulating the photophysical property of organic/polymer optical agents for promoted cancer phototheranostics. *Adv. Mater.* **2019**, *31*, 1806331.

(6) Qi, J.; Chen, C.; Zhang, X.; Hu, X.; Ji, S.; Kwok, R. T. K.; Lam, J. W. Y.; Ding, D.; Tang, B. Z. Light-driven transformable optical agent with adaptive functions for boosting cancer surgery outcomes. *Nat. Commun.* **2018**, *9*, 1848.

(7) Ni, X.; Zhang, X.; Duan, X.; Zheng, H.-L.; Xue, X.-S.; Ding, D. Near-infrared afterglow luminescent aggregation-induced emission dots with ultrahigh tumor-to-liver signal ratio for promoted image-guided cancer surgery. *Nano Lett.* **2019**, *19*, 318−330.

(8) Gao, H.; Zhang, X.; Chen, C.; Li, K.; Ding, D. Unity makes strength: how aggregation-induced emission luminogens advance the biomedical field. *Adv. Biosyst.* **2018**, *2*, 1800074.

(9) Mi, P.; Kokuryo, D.; Cabral, H.; Wu, H.; Terada, Y.; Saga, T.; Aoki, I.; Nishiyama, N.; Kataoka, K. A pH-activatable nanoparticle with signal-amplification capabilities for non-invasive imaging of tumour malignancy. *Nat. Nanotechnol.* **2016**, *11*, 724.

(10) Shimada, K.; Isoda, H.; Hirokawa, Y.; Arizono, S.; Shibata, T.; Togashi, K. Comparison of gadolinium-EOB-DTPA-enhanced and diffusion-weighted liver MRI for detection of small hepatic metastases. *Eur. Radiol.* **2010**, *20*, 2690−2698.

(11) Ahn, S. S.; Kim, M.-J.; Lim, J. S.; Hong, H.-S.; Chung, Y. E.; Choi, J.-Y. Added value of gadoxetic acid-enhanced hepatobiliary phase MR imaging in the diagnosis of hepatocellular carcinoma. *Radiology* **2010**, *255*, 459−466.

(12) Zhang, Q.; Yin, T.; Gao, G.; Shapter, J. G.; Lai, W.; Huang, P.; Qi, W.; Song, J.; Cui, D. Multifunctional core@shell magnetic nanoprobes for enhancing targeted magnetic resonance imaging and fluorescent labeling *in vitro* and *in vivo*. *ACS Appl. Mater. Interfaces* **2017**, *9*, 17777−17785.

(13) Wang, F.; Xue, X.; Liu, X. Multicolor tuning of (Ln, P)-doped YVO_4 nanoparticles by single-wavelength excitation. *Angew. Chem., Int. Ed.* **2008**, *47*, 906−909.

(14) Liu, J.; Li, Y. General synthesis of colloidal rare earth orthovanadate nanocrystals. *J. Mater. Chem.* **2007**, *17*, 1797−1803.

(15) Liu, J.; Li, Y. D. Synthesis and self-assembly of luminescent Ln^{3+}-doped $LaVO_4$ uniform nanocrystals. *Adv. Mater.* **2007**, *19*, 1118−1122.

(16) Gupta, B. K.; Rathee, V.; Narayanan, T. N.; Thanikaivelan, P.; Saha, A.; Govind, S.; Singh, S. P.; Shanker, V.; Marti, A. A.; Ajayan, P. M. Probing a bifunctional luminomagnetic nanophosphor for biological applications: a photoluminescence and time-resolved spectroscopic study. *Small* **2011**, *7*, 1767−1773.

(17) Anitha, M.; Ramakrishnan, P.; Chatterjee, A.; Alexander, G.; Singh, H. Spectral properties and emission efficiencies of $GdVO_4$ phosphors. *Appl. Phys. A: Mater. Sci. Process.* **2002**, *74*, 153−162.

(18) Xin, H.; Lin, L.-X.; Wu, J.-H.; Yan, B. Hydrothermal synthesis and multi-color photoluminescence of GdVO$_4$: Ln^{3+} (Ln= Sm, Dy, Er) sub-micrometer phosphors. *J. Mater. Sci.: Mater. Electron.* **2011**, *22*, 1330−1334.

(19) Bolles, G. M.; Yazdani, M.; Stalcup, S. T.; Creeden, S. G.; Collins, H. R.; Nietert, P. J.; Roberts, D. R. Development of high signal intensity within the globus pallidus and dentate nucleus following multiple administrations of gadobenate dimeglumine. *Am. J. Neuroradiol.* **2018**, *39*, 415−420.

(20) McDonald, R. J.; McDonald, J. S.; Kallmes, D. F.; Jentoft, M. E.; Paolini, M. A.; Murray, D. L.; Williamson, E. E.; Eckel, L. J. Gadolinium deposition in human brain tissues after contrast-enhanced MR imaging in adult patients without intracranial abnormalities. *Radiology* **2017**, *285*, 546−554.

(21) Dong, H.; Du, S.-R.; Zheng, X.-Y.; Lyu, G.-M.; Sun, L.-D.; Li, L.-D.; Zhang, P.-Z.; Zhang, C.; Yan, C.-H. Lanthanide nanoparticles: from design toward bioimaging and therapy. *Chem. Rev.* **2015**, *115*, 10725−10815.

(22) Ahmad, M. W.; Kim, C. R.; Baeck, J. S.; Chang, Y.; Kim, T. J.; Bae, J. E.; Chae, K. S.; Lee, G. H. Bovine serum albumin (BSA) and cleaved-BSA conjugated ultrasmall Gd$_2$O$_3$ nanoparticles: Synthesis, characterization, and application to MRI contrast agents. *Colloids Surf., A* **2014**, *450*, 67−75.

(23) Fang, J.; Chandrasekharan, P.; Liu, X.-L.; Yang, Y.; Lv, Y.-B.; Yang, C.-T.; Ding, J. Manipulating the surface coating of ultra-small Gd$_2$O$_3$ nanoparticles for improved T_1-weighted MR imaging. *Biomaterials* **2014**, *35*, 1636−1642.

(24) Tian, Y.; Yang, H.-Y.; Li, K.; Jin, X. Monodispersed ultrathin GdF$_3$ nanowires: oriented attachment, luminescence, and relaxivity for MRI contrast agents. *J. Mater. Chem.* **2012**, *22*, 22510−22516.

(25) Xing, H.; Zhang, S.; Bu, W.; Zheng, X.; Wang, L.; Xiao, Q.; Ni, D.; Zhang, J.; Zhou, L.; Peng, W.; Zhao, K.; Hua, Y.; Shi, J. Ultrasmall NaGdF$_4$ nanodots for efficient MR angiography and atherosclerotic plaque imaging. *Adv. Mater.* **2014**, *26*, 3867−3872.

(26) Hou, Y.; Qiao, R.; Fang, F.; Wang, X.; Dong, C.; Liu, K.; Liu, C.; Liu, Z.; Lei, H.; Wang, F.; Gao, M. NaGdF$_4$ nanoparticle-based molecular probes for magnetic resonance imaging of intraperitoneal tumor xenografts *in vivo*. *ACS Nano* **2013**, *7*, 330−338.

(27) Huang, S.; Liu, J.; Liu, D.; Yuan, Q. Facile and large-scale synthesis of Gd(OH)$_3$ nanorods for MR imaging with low toxicity. *New J. Chem.* **2012**, *36*, 1335−1338.

(28) Dong, K.; Ju, E.; Liu, J.; Han, X.; Ren, J.; Qu, X. Ultrasmall biomolecule-anchored hybrid GdVO$_4$ nanophosphors as a metabolizable multimodal bioimaging contrast agent. *Nanoscale* **2014**, *6*, 12042−12049.

(29) Yin, W.; Zhou, L.; Gu, Z.; Tian, G.; Jin, S.; Yan, L.; Liu, X.; Xing, G.; Ren, W.; Liu, F.; Pan, Z.; Zhao, Y. Lanthanide-doped GdVO$_4$ upconversion nanophosphors with tunable emissions and their applications for biomedical imaging. *J. Mater. Chem.* **2012**, *22*, 6974−6981.

(30) Ren, W.; Tian, G.; Zhou, L.; Yin, W.; Yan, L.; Jin, S.; Zu, Y.; Li, S.; Gu, Z.; Zhao, Y. Lanthanide ion-doped GdPO$_4$ nanorods with dual-modal bio-optical and magnetic resonance imaging properties. *Nanoscale* **2012**, *4*, 3754−3760.

(31) Rodriguez-Liviano, S.; Nuñez, N. O.; Rivera-Fernández, S.; De la Fuente, J. M.; Ocaña, M. Ionic liquid mediated synthesis and surface modification of multifunctional mesoporous Eu:GdF$_3$ nanoparticles for biomedical applications. *Langmuir* **2013**, *29*, 3411−3418.

(32) Bouzigues, C.; Gacoin, T.; Alexandrou, A. Biological applications of rare-earth based nanoparticles. *ACS Nano* **2011**, *5*, 8488−8505.

(33) Yi, S. S.; Bae, J. S.; Shim, K. S.; Moon, B. K.; Seo, H. J.; Jeong, J. H.; Kim, J. H. Photoluminescence behaviors of Eu-doped GdVO$_4$ thin film phosphors grown by pulsed laser ablation. *J. Alloys Compd.* **2006**, *408−412*, 890−893.

(34) Escudero, A.; Carrillo-Carrión, C.; Zyuzin, M. V.; Ashraf, S.; Hartmann, R.; Núñez, N. O.; Ocaña, M.; Parak, W. J. Synthesis and functionalization of monodisperse near-ultraviolet and visible excitable multifunctional Eu^{3+}, Bi^{3+}:REVO$_4$ nanophosphors for bioimaging and biosensing applications. *Nanoscale* **2016**, *8*, 12221−12236.

(35) Park, W.; Jung, M.; Yoon, D. Influence of Eu^{3+}, Bi^{3+} co-doping content on photoluminescence of YVO$_4$ red phosphors induced by ultraviolet excitation. *Sens. Actuators, B* **2007**, *126*, 324−327.

(36) Xu, Q.; Lin, B.; Mao, Y. Photoluminescence characteristics of energy transfer between Er^{3+} and Bi^{3+} in Gd$_2$O$_3$: Er^{3+}, Bi^{3+}. *J. Lumin.* **2008**, *128*, 1965−1968.

(37) Takeshita, S.; Isobe, T.; Niikura, S. Low-temperature wet chemical synthesis and photoluminescence properties of YVO$_4$: Bi^{3+}, Eu^{3+} nanophosphors. *J. Lumin.* **2008**, *128*, 1515−1522.

(38) Lenczewska, K.; Gerasymchuk, Y.; Vu, N.; Liem, N. Q.; Boulon, G.; Hreniak, D. The size effect on the energy transfer in Bi^{3+}−Eu^{3+} co-doped GdVO$_4$ nanocrystals. *J. Mater. Chem. C* **2017**, *5*, 3014−3023.

(39) Szczeszak, A.; Grzyb, T.; Śniadecki, Z.; Andrzejewska, N.; Lis, S.; Matczak, M.; Nowaczyk, G.; Jurga, S.; Idzikowski, B. Structural, spectroscopic, and magnetic properties of Eu^{3+}-doped GdVO$_4$ nanocrystals synthesized by a hydrothermal method. *Inorg. Chem.* **2014**, *53*, 12243−12252.

(40) Gavrilović, T. V.; Jovanović, D. J.; Lojpur, V.; Dramićanin, M. D. Multifunctional Eu^{3+}-and Er^{3+}/Yb^{3+}-doped GdVO$_4$ nanoparticles synthesized by reverse micelle method. *Sci. Rep.* **2015**, *4*, 4209.

(41) Mahalley, B. N.; Pode, R. B.; Gupta, P. K. Synthesis of GdVO$_4$: Bi, Eu red phosphor by combustion process. *Phys. Status Solidi A* **2000**, *177*, 293−302.

(42) Wang, C.; Tao, H.; Cheng, L.; Liu, Z. Near-infrared light induced *in vivo* photodynamic therapy of cancer based on upconversion nanoparticles. *Biomaterials* **2011**, *32*, 6145−6154.

(43) Li, X.; Zhang, F.; Zhao, D. Highly efficient lanthanide upconverting nanomaterials: progresses and challenges. *Nano Today* **2013**, *8*, 643−676.

(44) Yang, Q.; Li, X.; Xue, Z.; Li, Y.; Jiang, M.; Zeng, S. Short-wave near-infrared emissive GdPO$_4$:Nd^{3+} theranostic probe for in vivo bioimaging beyond 1300 nm. *RSC Adv.* **2018**, *8*, 12832−12840.

(45) Xu, W.; Wang, Y.; Bai, X.; Dong, B.; Liu, Q.; Chen, J.; Song, H. Controllable Synthesis and Size-Dependent Luminescent Properties of YVO$_4$:Eu^{3+} Nanospheres and Microspheres. *J. Phys. Chem. C* **2010**, *114*, 14018−14024.

(46) Riwotzki, K.; Haase, M. Wet-chemical synthesis of doped colloidal nanoparticles: YVO$_4$:Ln (Ln = Eu, Sm, Dy). *J. Phys. Chem. B* **1998**, *102*, 10129−10135.

(47) Chen, D.; Yu, Y.; Huang, P.; Lin, H.; Shan, Z.; Zeng, L.; Yang, A.; Wang, Y. Color-tunable luminescence for Bi^{3+}/Ln^{3+}: YVO$_4$ (Ln=Eu, Sm, Dy, Ho) nanophosphors excitable by near-ultraviolet light. *Phys. Chem. Chem. Phys.* **2010**, *12*, 7775−7778.

(48) Wu, M.; Li, L.; Yu, X.; Zhang, D.; Sun, T.; Li, X.; Sun, L.; Lui, S.; Huang, X.; Bi, F.; Wang, H.; Zhu, H.; Gong, Q. Multifunctional layered gadolinium hydroxide nanoplates for ultrahigh field magnetic resonance imaging, computed tomography and fluorescence bioimaging. *J. Biomed. Nanotechnol.* **2014**, *10*, 3620−3630.

(49) Chen, F.; Bu, W.; Zhang, S.; Liu, J.; Fan, W.; Zhou, L.; Peng, W.; Shi, J. Gd^{3+}-ion-doped upconversion nanoprobes: relaxivity mechanism probing and sensitivity optimization. *Adv. Funct. Mater.* **2013**, *23*, 298−307.

(50) Lee, M.-J.; Kim, M.-J.; Yoon, C.-S.; Song, S. Y.; Park, K.; Kim, W. S. The T_2-shortening effect of gadolinium and the optimal conditions for maximizing the CNR for evaluating the biliary system: a phantom study. *Korean J. Radiol.* **2011**, *12*, 358−364.

(51) Hu, H.; Liu, S.; Li, D.; Wang, M.; Moats, R.; Shan, H.; Conti, P. S.; Li, Z. The synthesis of lanthanide-doped GdVO$_4$ ultrathin nanosheets with great optical and paramagnetic properties for FRET biodetection and *in vivo* MR imaging. *J. Mater. Chem. B* **2014**, *2*, 3998−4007.

(52) Yim, H.; Yang, S.-G.; Jeon, Y. S.; Park, I. S.; Kim, M.; Lee, D. H.; Bae, Y. H.; Na, K. The performance of gadolinium diethylene triamine pentaacetate-pullulan hepatocyte-specific T_1 contrast agent for MRI. *Biomaterials* **2011**, *32*, 5187−5194.

(53) Liu, C.; Hou, Y.; Gao, M. Are rare-earth nanoparticles suitable for *in vivo* applications? *Adv. Mater.* **2014**, *26*, 6922−6932.

(54) Xiang, Y.; Yu, X.-F.; He, D.-F.; Sun, Z.; Cao, Z.; Wang, Q.-Q. Synthesis of highly luminescent and anion-exchangeable cerium-doped layered Yttrium hydroxides for sensing and photofunctional applications. *Adv. Funct. Mater.* **2011**, *21*, 4388−4396.

(55) Song, K. D.; Choi, D.; Lee, J. H.; Im, G. H.; Yang, J.; Kim, J.-H.; Lee, W. J. Evaluation of tumor microvascular response to brivanib by dynamic contrast-enhanced 7-*T* MRI in an orthotopic xenograft model of hepatocellular carcinoma. *Am. J. Roentgenol.* **2014**, *202*, W559−W566.